

OPEN ACCESS

EDITED BY Yangxing Zheng, Florida State University, United States

REVIEWED BY
Jiepeng Chen,
Chinese Academy of Sciences (CAS), China
Rui Sun,
University of California, San Diego,
United States

*CORRESPONDENCE
Toshiaki Shinoda

☑ toshiaki.shinoda@tamucc.edu

RECEIVED 24 January 2023 ACCEPTED 23 June 2023 PUBLISHED 12 July 2023

CITATION

Shinoda T, Han W and Feng X (2023) Air-sea flux and SST variability associated with atmospheric rivers in the southeast Indian Ocean. *Front. Clim.* 5:1150785. doi: 10.3389/fclim.2023.1150785

COPYRIGHT

© 2023 Shinoda, Han and Feng. This is an open-access article distributed under the terms of the Creative Commons Attribution License (CC BY). The use, distribution or reproduction in other forums is permitted, provided the original author(s) and the copyright owner(s) are credited and that the original publication in this journal is cited, in accordance with accepted academic practice. No use, distribution or reproduction is permitted which does not comply with these terms.

Air-sea flux and SST variability associated with atmospheric rivers in the southeast Indian Ocean

Toshiaki Shinoda^{1*}, Weiqing Han² and Xue Feng¹

¹Department of Physical and Environmental Sciences, Texas A&M University-Corpus Christi, Corpus Christi, TX, United States, ²Department of Atmospheric and Oceanic Sciences, University of Colorado, Boulder, CO, United States

A previous study demonstrated that atmospheric rivers (ARs) generate substantial air-sea fluxes in the northeast Pacific. Since the southeast Indian Ocean is one of the active regions of ARs, similar air-sea fluxes could be produced. However, the spatial pattern of sea surface temperature (SST) in the southeast Indian Ocean, especially along the west coast of Australia, is different from that in the northeast Pacific because of the poleward flowing Leeuwin Current, which may cause different air-sea fluxes. This study investigates AR-associated air-sea fluxes in the southeast Indian Ocean and their relation with SST variability. The large-scale spatial pattern of latent heat flux (evaporation) associated with ARs in the southeast Indian Ocean is similar to that in the northeast Pacific. A significant difference is however found near the coastal area where relatively warm SSTs are maintained in all seasons. While AR-induced latent heat flux is close to zero around the west coast of North America where the equatorward flowing coastal current and upwelling generate relatively cold SSTs, a significant latent heat flux induced by ARs is evident along the west coast of Australia due to the relatively warm surface waters. Temporal variations of coastal air-sea fluxes associated with landfalling ARs are investigated based on the composite analysis. While the moisture advection reduces the latent heat during landfalling, the reduction of air humidity with strong winds enhances large evaporative cooling (latent heat flux) after a few days of the landfalling. A significant SST cooling along the coast is found due to the enhanced latent heat flux.

KEYWORDS

atmospheric rivers, air-sea flux, Indian Ocean, Leeuwin Current, air-sea interaction

1. Introduction

Atmospheric rivers (ARs) are narrow elongated regions of large water vapor contents and strong winds in the lower troposphere, which are responsible for the majority of large-scale meridional water vapor transport over the globe (Zhu and Newell, 1998; Gimeno et al., 2014). ARs deliver much of the water vapor from the tropical oceans to the western side of continents, and are often responsible for major floods and storms in many areas including the west coast of North America and northern Europe. Because of the socioeconomic importance of ARs, hydrological impacts of ARs such as extreme precipitation and snowpack in these regions were intensively studied in the last few decades (e.g., Persson et al., 2005; Ralph et al., 2005, 2006; Neiman et al., 2008; Smith et al., 2010; Dettinger et al., 2011; Doyle et al., 2014; Kim et al., 2015; Reynolds et al., 2019).

ARs are generally associated with surface cold fronts in the midlatitudes, and strong low-level winds near the AR center are often connected to the warm sector of extratropical cyclones. Because of strong surface winds in the vicinity of the AR center (e.g., Waliser and Guan, 2017), large air-sea fluxes including surface evaporation can be generated and in turn influence moisture budget of ARs. However, until recently, AR-associated air-sea fluxes, especially over the open ocean areas, have received little attention since previous studies mostly focused on hydrological components of ARs in the coastal areas such as heavy precipitation, flooding, and moisture transport produced by landfalling ARs.

Recent studies demonstrate that strong winds associated with ARs generate substantial air-sea fluxes and ocean variability in the northeast Pacific (Shinoda et al., 2019). Shinoda et al. (2019) described the spatial variations of surface evaporation (and thus latent heat flux) produced by AR-induced surface winds in the northeast Pacific, and demonstrated that prominent evaporation is generated only on the western poleward side of AR upstream area where winds are strong and air humidity is relatively low while the evaporation is relatively weak around the AR center because of the high air humidity. They also suggest that such spatial pattern of surface evaporation and associated winds may affect the moisture budget around the AR center since westerly winds around the area of maximum evaporation could bring the surface moisture toward the region of high moisture near the AR center (Supplementary Figure S1). In addition, AR-induced large latent heat flux can generate strong sea surface temperature (SST) fluctuations, which may in turn affect the atmospheric variability.

While previous studies demonstrated the potentially important role of air-sea fluxes in the moisture budget associated with ARs for the northeast Pacific, there are not yet comprehensive studies on AR-associated air-sea fluxes in other areas. Although ARs are active in mid-latitudes over all major ocean basins (e.g., Guan and Waliser, 2015; Hirota et al., 2016; Mundhenk et al., 2016; Guo et al., 2020), characteristics of AR and associated air-sea fluxes could be different because of the different climatological surface winds and SST fields. For example, the spatial structure of AR-associated low-level winds is significantly different in the Northern and Southern Hemispheres (Guo et al., 2020). In the Southern Hemisphere, stronger zonal winds associated with ARs are found in the areas of cyclonic circulation because the climatological circulation is more zonally symmetric (Guo et al., 2020).

The southeast Indian Ocean is one of the areas where ARs are relatively active (e.g., Guan and Waliser, 2015; Guan et al., 2018), and ARs in this region often make landfall on the west coast of Australia (Shinoda et al., 2020). While the west coast of Australia is located on the eastern side of the ocean basin like the west coast of North America, climatological SST fields in the southeast Indian Ocean are unique in that relatively warm SSTs are found due to the poleward flowing Leeuwin Current (e.g., Cresswell and Golding, 1980; Feng et al., 2003, 2008). SSTs in the southeast Indian Ocean near the coast of Australia are much warmer than eastern boundaries of other ocean basins at comparable latitudes (e.g., Feng et al., 2003). For example, SSTs along the west coast of North America are 4-5°C colder than the west coast of Australia at the same latitude (Supplementary Figure S2). Also, the equatorward winds are observed along the west coast of Australia almost all year round, which bring the colder air to this region. As a result, the air-sea temperature difference is largely enhanced by the Leeuwin Current which flows poleward against equatorward local winds. In contrast, the equatorward flowing California Current reduces the air-sea temperature difference along the west coast of North America. Accordingly, the climatological air-sea temperature difference along the west coast of Australia is much larger (\sim 1–2°C) than that along the west coast of North America (Supplementary Figure S2, bottom panels).

The mean and variability of air-sea fluxes in the southeast Indian Ocean are largely influenced by the Leeuwin Current which carries warm waters from the tropical western Pacific and eastern Indian Ocean to the west coast of Australia (Feng and Shinoda, 2019). Because of the unique SST and air-sea temperature difference caused by the Leeuwin Current, the evolution of AR-induced air-sea fluxes over the southeast Indian Ocean could be different from that in other regions including the northeast Pacific.

The dynamical ocean response to ARs over the southeast Indian Ocean such as the influence on the Leeuwin Current has been examined in a recent study (Shinoda et al., 2020). Because of the strong winds associated with ARs, the Leeuwin Current is accelerated during a few days when ARs making landfall, which is associated with a substantial sea level rise along the coast. Although such AR-associated strong winds can generate large air-sea fluxes, they have not yet been quantified in previous studies as Shinoda et al. (2020) did not discuss the thermodynamical response to ARs.

A major purpose of this study is to quantify air-sea flux and SST associated with ARs over the southeast Indian Ocean based on the analysis of global datasets of air-sea fluxes and AR characteristics. In particular, the role of relatively warm SSTs maintained by the poleward flowing Leeuwin Current is emphasized. Analyses similar to our previous study (Shinoda et al., 2019) have been performed for the southeast Indian Ocean, and the results are compared with those in the northeast Pacific to discuss differences and similarities over these regions.

2. Data and methods

Datasets and primary methods used for the analysis are described in this section. Since the results will be compared with those for the northeast Pacific, the data and methods similar to those used by Shinoda et al. (2019) are mostly employed in this study.

2.1. Air-sea fluxes and surface atmospheric variables

Daily mean values of air-sea fluxes and other surface variables obtained from the Objectively Analyzed air-sea Fluxes (OAFlux) products (Yu et al., 2008) are analyzed to describe AR-associated fluxes and SSTs. These include surface evaporation, latent and sensible heat fluxes, specific humidity at 2 m height, wind speed at 10 m height, and SST. The data are provided on a $1^{\circ} \times 1^{\circ}$ grid. Also, daily mean winds at 10 m height on a $0.25^{\circ} \times 0.25^{\circ}$ grid from Cross-Calibrated Multi-Platform wind vector analysis (CCMP) Version 3.0 (Atlas et al., 2011; Mears et al., 2022a,b) are used for describing wind vectors near the surface. Surface shortwave and

longwave radiation is derived from the Clouds and the Earth's Radiant Energy System (CERES). Anomalies of variables derived from the OAFlux are calculated by subtracting the climatological seasonal cycle for the period 2001–2015.

2.2. Compositing method

Composites of air-sea fluxes, surface atmospheric variables, and SST are constructed using the global AR data set created by Guan and Waliser (2015) in which AR events are identified based on the characteristics of the integrated water vapor transport (IVT) at 6 hourly intervals. The method is previously used in recent studies on ARs (Shinoda et al., 2019, 2020; Guo et al., 2020).

In the algorithm developed by Guan and Waliser (2015), grid points with enhanced IVT are first identified using the criteria in which the IVT intensity exceeds the seasonally and geographically varying 85th percentile, or a fixed limit of 100 kg m $^{-1}$ s $^{-1}$, whichever is greater. Then further constraints of AR conditions are applied to identify ARs. These include the coherence in IVT direction across individual grid points, mean IVT having a poleward component, consistency between mean IVT direction and the AR shape orientation and geometric requirements (length > 2,000 km and length-to-width ratio >2). Further details are found in Guan and Waliser (2015).

In this study, the composite evolution of variables related to air-sea fluxes such as surface evaporation and SST are constructed using the location of AR centroid and IVT intensity at the AR center derived by Guan and Waliser (2015). To examine the air-sea flux and SST variability associated with ARs over the southeast Indian Ocean, relevant variables are composited around the AR centroid using all of the ARs in the domain 15°S-40°S, 70°E-120°E. Composites are formed by averaging the daily mean values of air-sea fluxes, SST and other relevant atmospheric variables of all identified AR events over a 40° latitude by 60° longitude domain centered at the AR centroid, using events for the period of 2011-2015. Since ARs are often identified multiple times within a day, the same daily values are used multiple times for the composite in this case. Only AR events in which IVT at the center exceeds 500 kg m⁻¹ s⁻¹ are used to exclude weak events. Note that some of the composites for the northeast Pacific shown in Shinoda et al. (2019) are recalculated using the latitudinal range $(15^{\circ}\text{N}-40^{\circ}\text{N})$ which is the same as that in this study $(15^{\circ}\text{S}-40^{\circ}\text{S})$, and they are included in some of the results in this study for the comparison. The results of the recalculation are nearly identical to those in Shinoda et al. (2019). A total of 158 AR events are used for the composite. Note that the definition of the AR event here is the "snapshot" AR, which is different from the traditional definition based on the entire lifecycle of ARs. Hence the 158 daily snapshots are used here to form the composite.

3. Results

3.1. Air-sea fluxes associated with individual AR event: case study

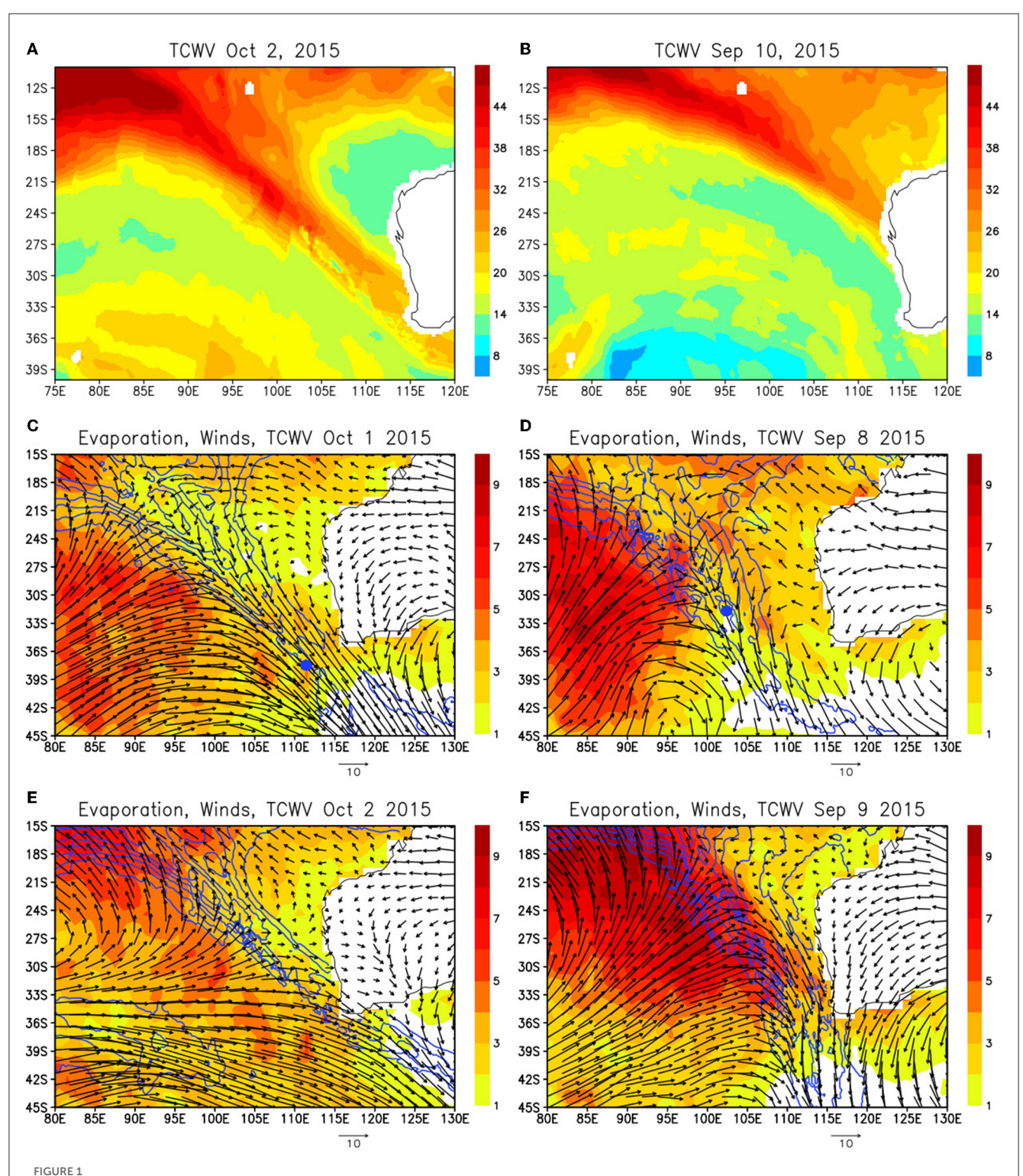
Air-sea flux and SST variability associated with two landfalling AR events are first investigated as case studies. Here, the results for the events in early October and early September, 2015 are discussed. The event in early October (September) made landfall on October 2 (September 9–10). These events are typical landfalling events often observed in the southeast Indian Ocean (Shinoda et al., 2020). Note that the dynamical ocean response to the event in early September such as the acceleration of the Leeuwin Current is thoroughly discussed in Shinoda et al. (2020).

Figure 1 shows the total column integrated water vapor (TCWV) (Figures 1A, B), surface evaporation, and winds (Figures 1C–F) during and right before these ARs made landfall in the southern part of the west coast of Australia. ARs are associated with a cyclonic circulation on the western poleward side of ARs and anti-cyclonic circulation on the eastern equatorward side of ARs (Figures 1C, D), which is common to many regions in the globe (Guo et al., 2020).

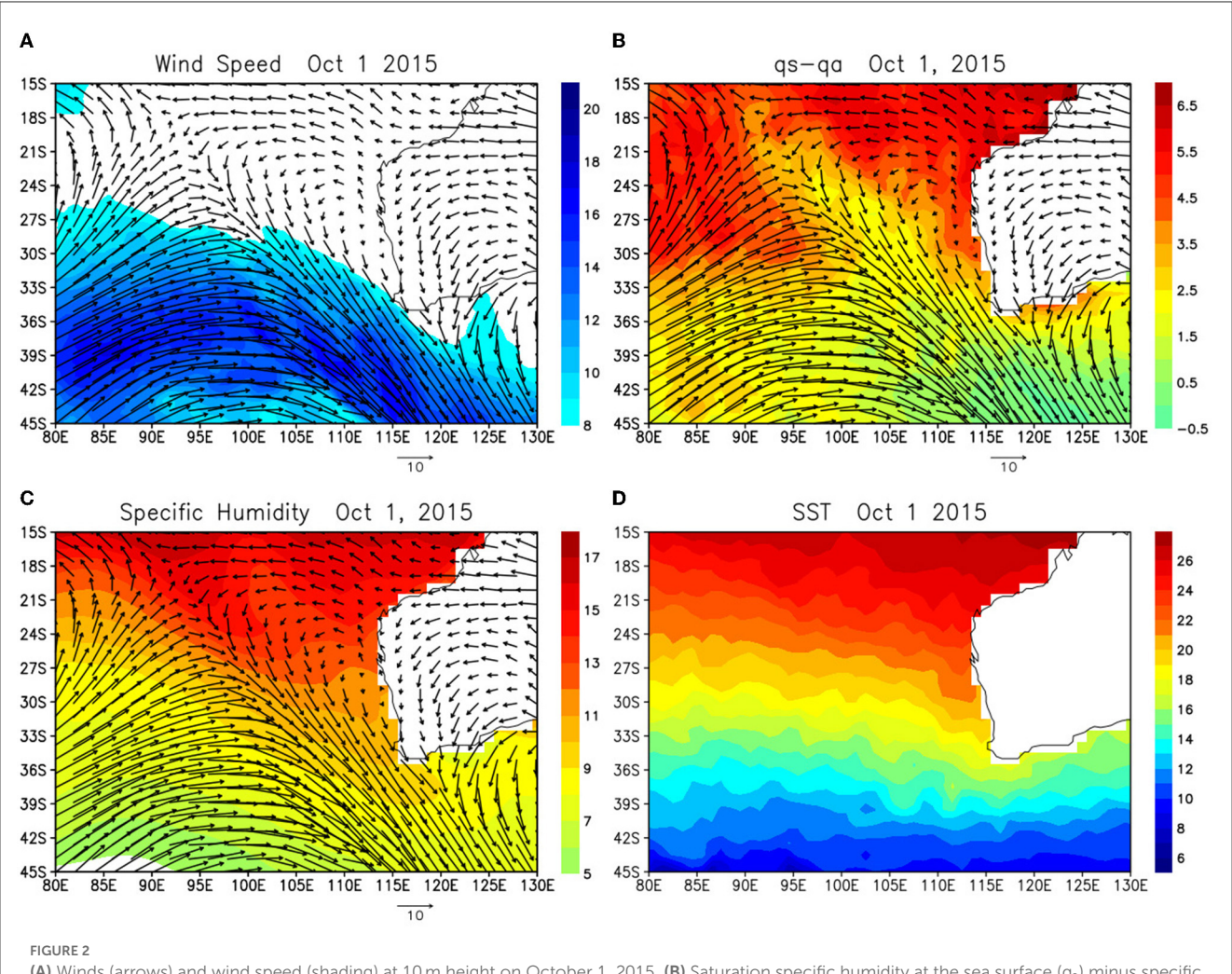
In association with the eastward movement of the high moisture region, strong northwesterlies associated with cyclonic circulations moved eastward and reached the coast when the ARs made landfall. Strong surface evaporation (and thus cooling due to surface latent heat flux) is found on the western poleward side of ARs whereas evaporation is small on the eastern equatorward side of ARs. These spatial patterns of evaporation relative to the AR center are determined by the wind speed, air humidity and SST. Surface winds exceed 12 m/s in a large area of the cyclonic circulation, and the maximum winds of about 20 m/s are found around the center of AR (Figure 2A). However, the specific humidity is also high near the AR center (Figures 2B, C), and thus the maximum evaporation is found on the western poleward side of AR where winds are still strong but the air is drier than the AR center. While winds are stronger in higher latitudes (south of 35°S), evaporation is generally much lower because of the colder SSTs (Figure 2D).

Overall spatial structure of the surface evaporation, winds and TCWV associated with ARs are consistent with that in the northeast Pacific at least qualitatively (Supplementary Figure S1). In particular, large evaporation is found on the western poleward side of AR where westerlies flow toward the AR center, which is evident in both the southeast Indian Ocean and northeast Pacific. Yet there are notable differences between the structure of these events described above and that in events in the northeast Pacific during CalWater 2015 field campaign reported in Shinoda et al. (2019). Relatively broad areas of strong evaporation are found in the western poleward side for the southeast Indian Ocean during these events while high evaporation areas are more confined in smaller areas in the northeast Pacific during the event in CalWater 2015 (Supplementary Figure S1).

While the large scale structure of evaporation and winds during these events is similar to that in the northeast Pacific, the prominent difference is found in the coastal areas. In the northeast Pacific, evaporation is close to zero north of around 30°N along the west coast of North America during the landfall because of the cold SST and high specific humidity (Supplementary Figure S1, see also Figure 4D in Shinoda et al., 2019). In contrast to such small evaporation along the west coast of North America, significant surface evaporation is found along the west coast of Australia at similar latitudes even where the air humidity is maximum. This is because the warmer SST along the coast due to the poleward flowing Leeuwin Current bringing warm waters from the tropics southward (Figure 2D). The air-sea fluxes and SSTs produced by



(A) Total column integrated water vapor (TCWV) (mm) on October 2, 2015 derived from Special Sensor Microwave Imager (SSMI) data. Adapted from Shinoda et al. (2020) (B) same as (A) except for September 10. Adapted from Shinoda et al. (2020) (C) surface evaporation (mm/day: shading), winds (m/s) at 10 m (arrows), and total column integrated water vapor (contour) on October 1, 2015. The contour starts from 20 mm and the interval is 4 mm. The blue mark indicates the location of the AR center identified based on the IVT criteria (D) same as (C) except for September 8. (E) Same as (C) except for October 2. (F) Same as (C) except for September 9.



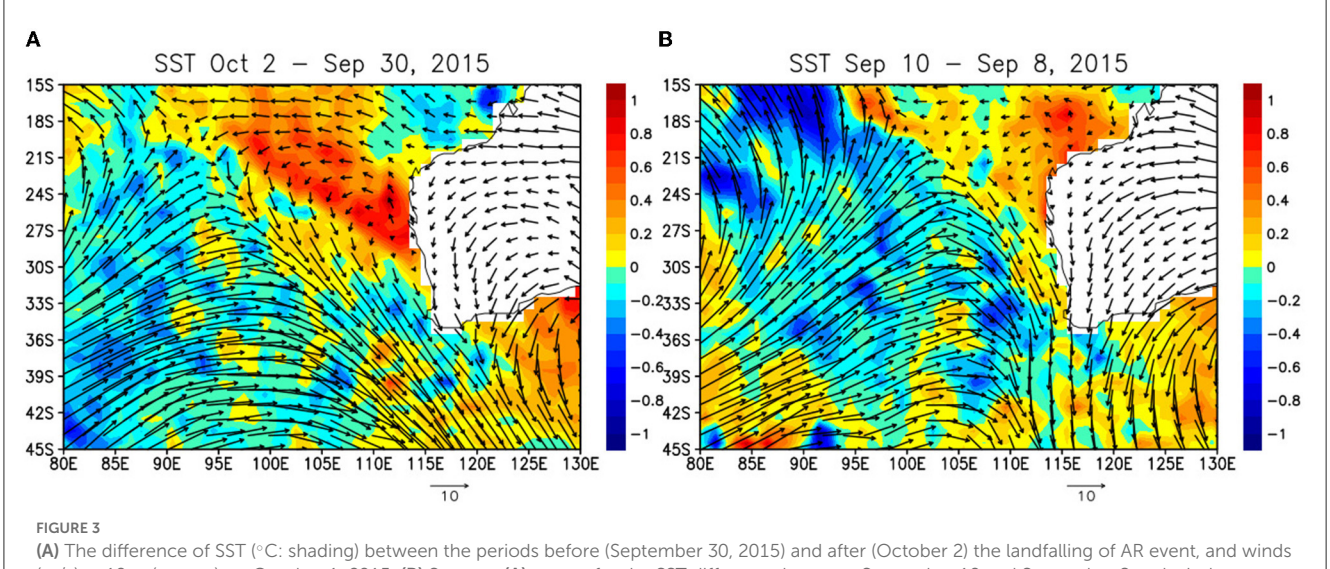
(A) Winds (arrows) and wind speed (shading) at 10 m height on October 1, 2015. (B) Saturation specific humidity at the sea surface (q_s) minus specific humidity at 2 m (q_a) (shading) from OAFlux, and winds (arrows) at 10 m height on October 1, 2015. (C) Same as (B) except for specific humidity (shading). (D) SST (shading) on October 1, 2015 from OAFlux.

ARs over the coastal areas are further discussed based on the composite analysis in the next section.

Because of the large (small) latent heat uptake on the western poleward (eastern equatorward) side of ARs, SST changes could be significantly different on the locations relative to the AR center. Figure 3 shows the SST difference between before and after the AR event. A significant cooling (warming) is found on the western poleward (eastern equatorward) side of ARs. Such spatial variations of SST changes are consistent with the net surface heat flux anomalies during these AR events (Figures 4A, B), suggesting that a significant portion of these SST changes is produced by surface heat fluxes. Although the duration of anomalous heat flux associated with ARs is only 2-4 days, the magnitude which exceeds 100 W/m² is sufficiently large for producing significant SST changes. The latent heat flux mostly contributes to the net surface heat flux as these fluxes show the similar spatial pattern (Figures 4C, D). While surface shortwave radiation shows a different spatial variation in which minimum values are found along the core of ARs, its amplitude is still significant and thus it also provides the warming on both sides of ARs (Figures 4E, F). During the event in early September, the negative net surface heat flux around the core of the AR is mostly generated by anomalous shortwave radiation (Figures 4B, F). However, the role of the reduction of shortwave radiation around the AR core may vary from event to event. The relatively minor contribution of the shortwave radiation near the AR core especially at lower latitudes (equatorward of 30°S) is found for the event in early October (Figure 4E).

3.2. Composite analysis

The case studies in the previous section suggest the similarities and differences in the air-sea flux and SST variability associated with ARs in the southeast Indian Ocean and the northeast Pacific. While many features such as the spatial pattern and evolution of surface variables are similar in most events, there are some differences in individual events such as that in the shortwave radiation between the early September and early October events. The case studies also suggest the prominent differences in the coastal areas for the landfalling ARs between the two regions. In this



(m/s) at 10 m (arrows) on October 1, 2015. **(B)** Same as **(A)** except for the SST difference between September 10 and September 8 and winds on September 9.

section, the results of the case studies are further confirmed based on the composite analysis. The analysis is discussed in separate sections for those in open ocean areas and near the coast.

3.2.1. Air-sea flux evolution in the open ocean area

Figure 5A shows the composites of evaporation, TCWV, and surface winds in the southeast Indian Ocean and those in the northeast Pacific (Figure 5B). Figure 5B is flipped upside down such that the direction of the North Pole is downward for the comparison between these two regions in different hemispheres. As shown in the case studies, large surface evaporation is found in the western poleward side of AR upstream areas. Near the AR center, evaporation is small because of the high specific air humidity even though winds are strong. Composites of SST tendency in the southeast Indian Ocean and the northeast Pacific are shown in Figures 5C, D, respectively. SST cooling (warming) is found on the western poleward (eastern equatorward) side of AR core, which is consistent with the case studies of individual events. Note that the magnitude of evaporation changes associated with ARs in the composite is statistically significant (Supplementary Figure S3).

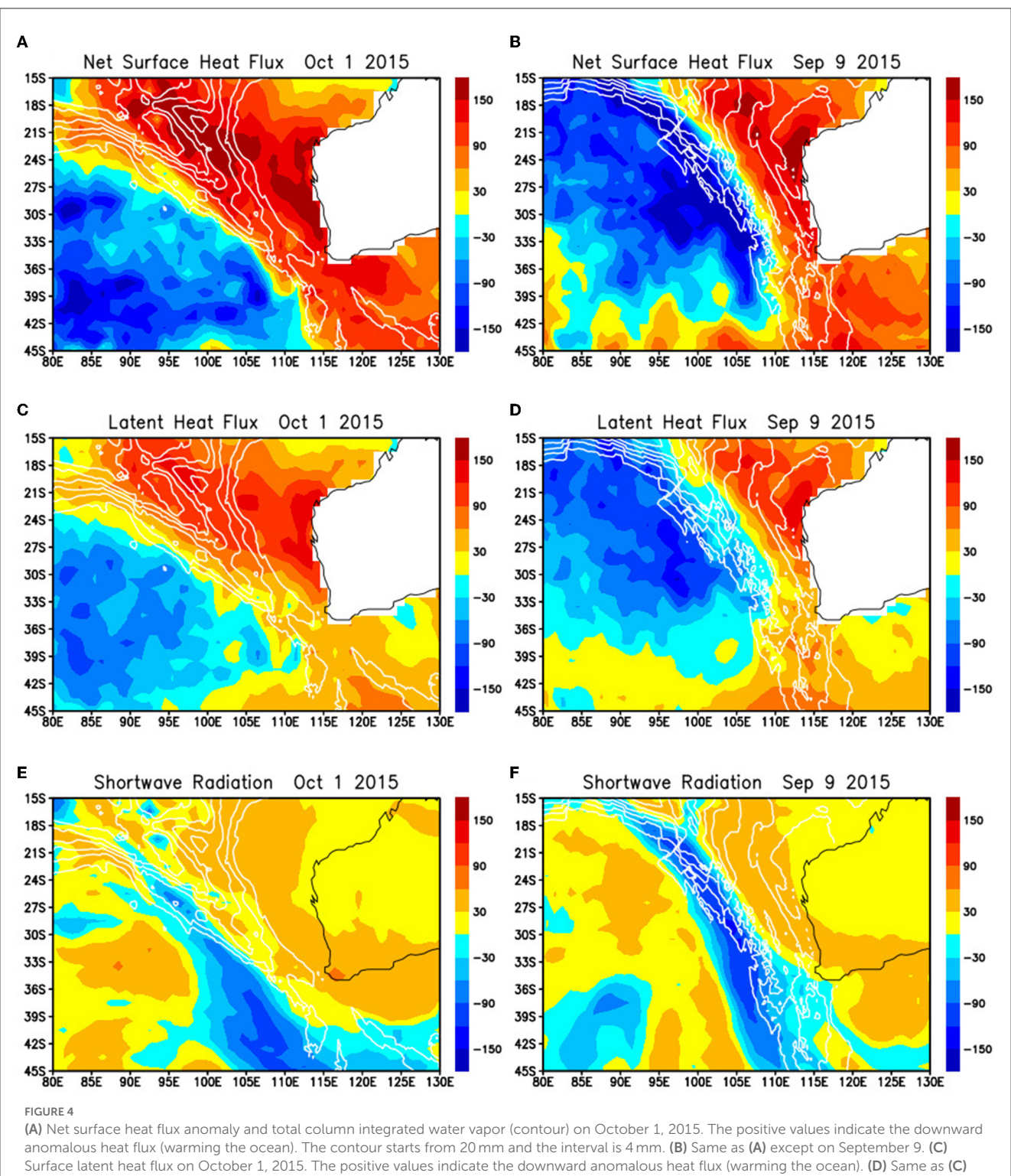
While the overall spatial structure of evaporation and SST tendency are similar in the southeast Indian Ocean and the northeast Pacific, there are some notable differences. The surface evaporation on the western poleward side is much stronger in the northeast Pacific and the zonal extent of the region of large evaporation is smaller. The associated SST cooling in these regions is stronger in the northeast Pacific. The difference in the magnitude of evaporation on the western poleward side is caused by the difference of the AR locations in the northeast Pacific and southeast Indian Ocean which are identified based on IVT characteristics. In the northeast Pacific, the center of AR events is located at lower latitudes (south of 35°N) more often than in the southeast Indian Ocean (not shown), and thus larger climatological evaporation (latent heat flux) due to the warmer SST is found in the vicinity

of the AR center. Such a difference in AR location between the two regions is primarily because the meridional component of surface winds associated ARs is weaker in the southeast Indian Ocean as shown in wind vectors in Figure 5 (see also Guo et al., 2020).

The anomalies of surface evaporation and SST tendency are shown in Figure 6. The magnitude of anomalous evaporation on the western poleward side of AR is comparable in both regions in contrast to the total evaporation shown in Figure 5 (Figures 6A, B). The maximum positive evaporation anomaly of about 1.7 mm/day is found in both regions. The magnitude and spatial variation of negative evaporation anomaly on the eastern equatorward side are also similar in both regions. Consistent with evaporation anomalies, the magnitude of SST tendency anomaly in the southeast Indian Ocean is comparable to that in the northeast Pacific. Yet there are some notable differences in the spatial structures of these anomalies. As in the total evaporation fields, the zonal extent of positive evaporation anomaly is larger in the southeast Indian Ocean. Also, the SST tendency anomalies in the northeast Pacific are more confined in the narrower region. This is also partly due to the difference in the spatial variation of winds in the two regions. The stronger zonal component of cyclonic circulation may cause the larger zonal extent for the regions of positive evaporation anomalies and SST cooling in the southeast Indian Ocean.

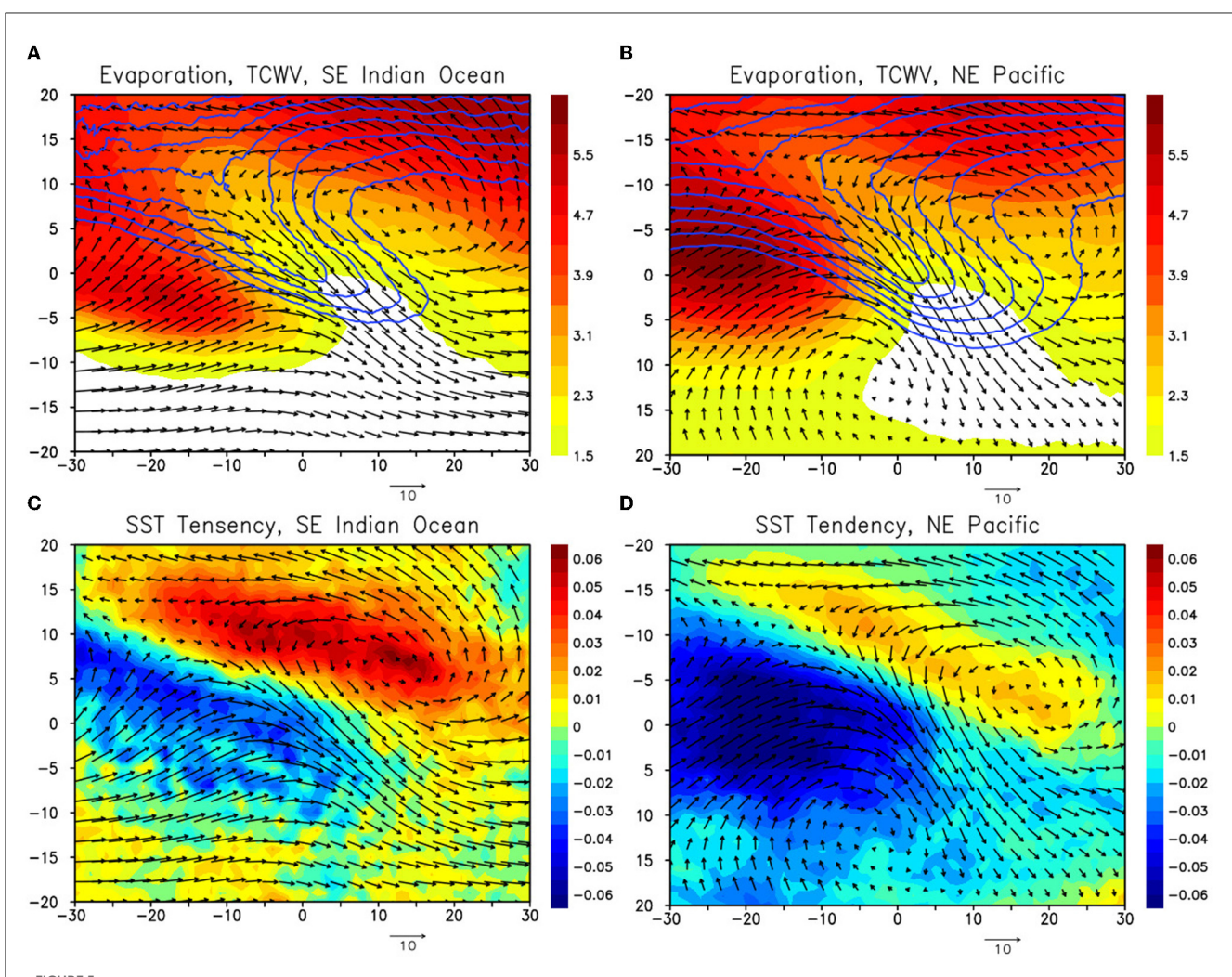
Consistent with the case studies, the spatial pattern of composite net surface heat flux anomaly is similar to that of SST tendency, and it is primarily determined by the latent heat flux (Figure 7). Shortwave radiation contributes to the warming on the eastern equatorward side of ARs. Although the magnitude of sensible heat flux anomaly is much smaller than the latent heat flux anomaly, it is not negligible for both the cooling and warming on western poleward side and eastern equatorward side of ARs.

The results described above suggest that a significant portion of AR-induced SST fluctuation is generated by surface heat fluxes and vertical processes. Although the overall spatial patterns of the SST tendency and net surface flux are similar, there are some differences



except on September 9. (E) Surface shortwave radiation on October 1, 2015. The positive values indicate the downward anomalous heat flux (warming the ocean). (F) Same as (E) except on September 9.

in their spatial structures, suggesting that oceanic processes may play a role in some areas in driving the SST variation. For example, a significant cooling of SST is found in the AR center while the net surface flux anomaly is nearly zero. The entrainment cooling caused by mixed layer deepening due to strong winds could partly generate the SST cooling in this region. However, further quantitative discussion on the relative importance of surface heat fluxes and other oceanic processes are not possible, given the large uncertainty of mixed layer depth in this region (e.g., Kataoka et al., 2017; Feng and Shinoda, 2019).



(A) Composite of evaporation (mm/day: shading), TCWV (mm: contour), and winds at 10 m (m/s: arrows) for the period 2011–2015 over the Southeast Indian Ocean (70°E–120°E, 15°S–40°S). The contour starts from 21 mm, and the interval is 3 mm. Horizontal (vertical) axis is longitude (latitude), in which 0° longitude, 0° latitude are defined as the location of the AR center. See text for the detail of the compositing method. (B) Same as (A) except for the Northeast Pacific (170°W–120°W, 15°N–40°N). The plot is flipped upside down such that the direction of the North Pole is downward to compare with (A). (C) Composite of SST tendency (C/day: shading) and winds at 10 m (m/s: arrows) for the period 2011–2015 over the Southeast Indian Ocean (70°E–120°E, 15°S–40°S). SST tendency is calculated as the difference between the 2-day average SST before and after the AR event. (D) Same as (C) except for the Northeast Pacific (170°W–120°W, 15°N–40°N). The plot is flipped upside down as in (B).

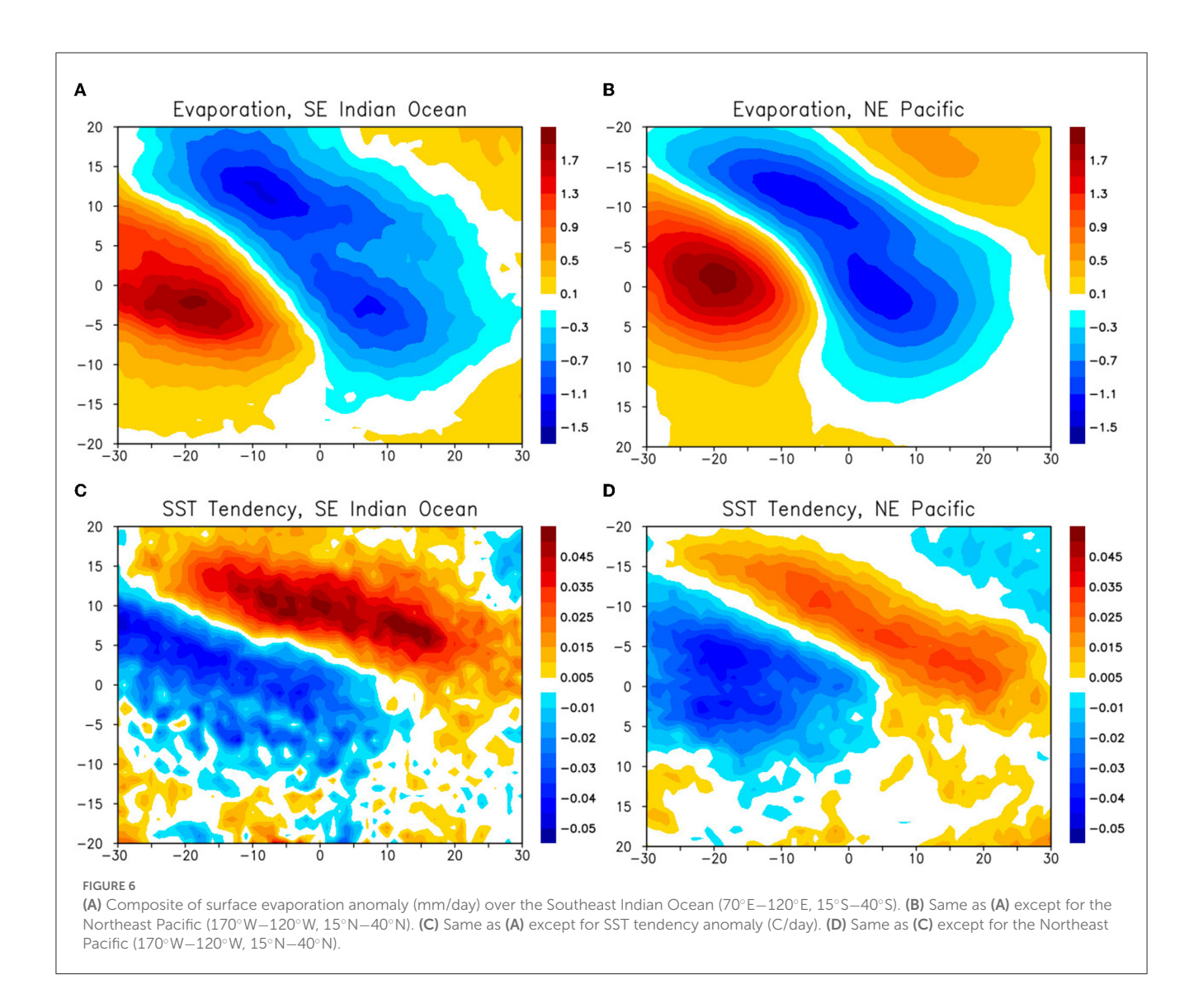
In summary, the composite analysis demonstrates that overall structures of air-sea fluxes and SST variability associated with ARs over the open ocean in the southeast Indian Ocean are consistent with those in the northeast Pacific. However, there are some notable differences such as the spatial structures of SST cooling and large evaporation on the western poleward side of AR, which is primarily due to the different spatial pattern of cyclonic circulations in these regions.

3.2.2. Evolution along the coast

The case studies described in Section 2 suggest that strong evaporation along the coast during AR landfalling is generated in the southeast Indian Ocean in contrast to the case of northeast Pacific where almost no evaporation is found along the coast of North America at similar latitudes (Figures 1E, F, Supplementary Figure S1). The results also suggest that the

significant evaporation along the coast in the southeast Indian Ocean is primarily due to the warm SST caused by the poleward flowing Leeuwin Current which carries warm waters from the equatorial areas. In this section, air-sea fluxes and SST fluctuations associated with ARs in the coastal areas are further examined based on the composite analysis.

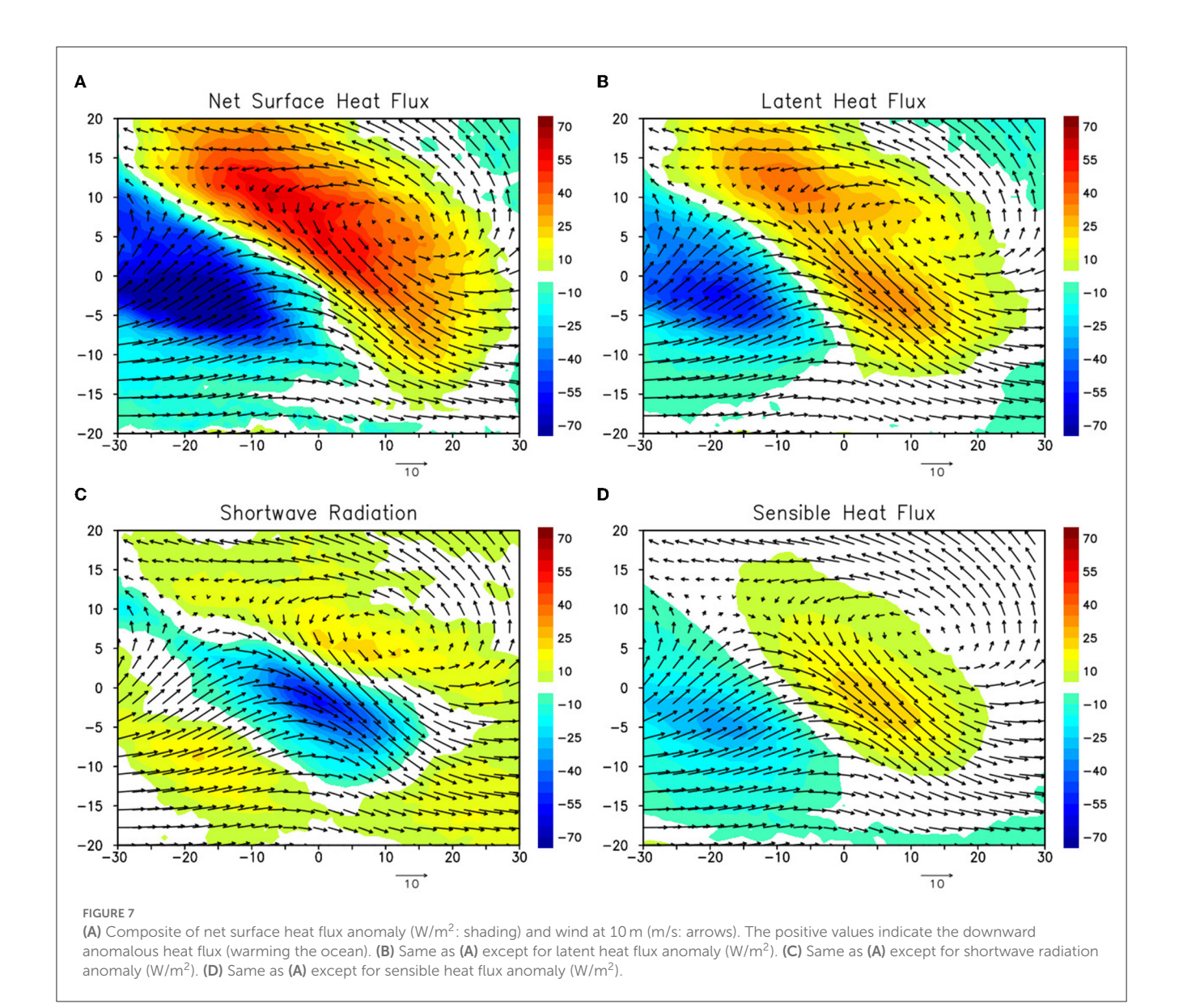
The composite of landfalling ARs is constructed using the method developed in Shinoda et al. (2019, 2020). As in the composite analysis for the entire southeast Indian Ocean (Section 3.2.1), the composite for the landfalling ARs is formed using the global AR data set in which ARs are objectively detected by the algorithm developed by Guan and Waliser (2015). The time and location of AR center and IVT at the AR center are included in the AR data set. The landfalling AR events along the west coast of Australia are identified as the event for which the AR center entered the area near the coast (35°S-25°S, 112°E-116.5°E) and made landfall (Shinoda et al., 2020). Composites are formed using



AR events for the period of 2011–2015, in which 67 landfalling AR events are identified. Hence 67 snapshots of ARs are used to construct the composite here. Further details of the compositing method are found in Shinoda et al. (2020).

Figure 8 shows the composite latent heat flux near the west coast of Australia. Here Day 0 indicates the day when the AR center is located close to the coast which is indicated by the area of the rectangular box in Figure 8A. The latent heat flux near the west coast of Australia south of 26°S exceeds 150 W/m² on Day 0 (Figure 8A). Such significant latent heat flux is not found along the coast of North America at similar latitudes (Shinoda et al., 2019; Bartusek et al., 2021). The latent heat flux is substantially enhanced on Day +3 which exceeds 220 W/m², and the significant latent heat flux of about 150 W/m² extends farther offshore of about 8–10° in longitude from the coast (Figure 8B). Despite the high air humidity at the coast on Day 0 due to the strong moisture transport by ARs, relatively warm SSTs (Figure 8C) could still maintain the significant vertical humidity gradient. Hence the strong winds associated with AR generate prominent latent heat fluxes. The spatial distribution of the SST reveals the influence of the southward flowing Leeuwin Current in which the maximum SST is found right near the coast where the current speed is maximum. Although the width of the Leeuwin Current is only 30–60 km, the warm waters carried by the Leeuwin Current in this region further spread offshore due primarily to active mesoscale eddies in this region (e.g., Chelton et al., 2007; Delman et al., 2018). Accordingly, relatively warm SSTs are found in the large areas near the coast compared to eastern boundaries in other ocean basins.

A substantial variation of latent heat flux and the associated SST fluctuation are further demonstrated by the time series of those averaged over the boxed area of Figures 8A, 9. As shown in Figure 8A, the latent heat flux is significant (\sim 130–140 W/m²) on Day -1 to Day 0 despite the specific humidity is maximum, which is caused the by the AR landfalling. This is because the SST is relatively warm (\sim 21.6°C) in contrast to the relatively cold SST (\sim 17°C) along the west coast of North America and winds are strong (\sim 8 m/s) during this period. Then the specific humidity rapidly decreases by 2 g/kg on Day +1–4 as ARs move eastward. During this period, wind speed remains to be strong (8–9 m/s), and thus the latent heat flux rapidly increases. On Day +3, the latent



heat flux reaches the maximum value of about 200 W/m². Hence during the 5-day period when ARs pass through the west coast of Australia, the latent heat flux varies by about 70 W/m², which is substantial compared to the climatological latent heat flux (~170 W/m²) around this region (e.g., Yu et al., 2008; Feng and Shinoda, on the analysis of the coast of the coast of the second second

2019). The SST cooling of about 0.15°C occurs in response to such large latent heat flux changes. However, the SST in this region could be influenced by other processes such as ocean dynamics which is further discussed in the payt section.

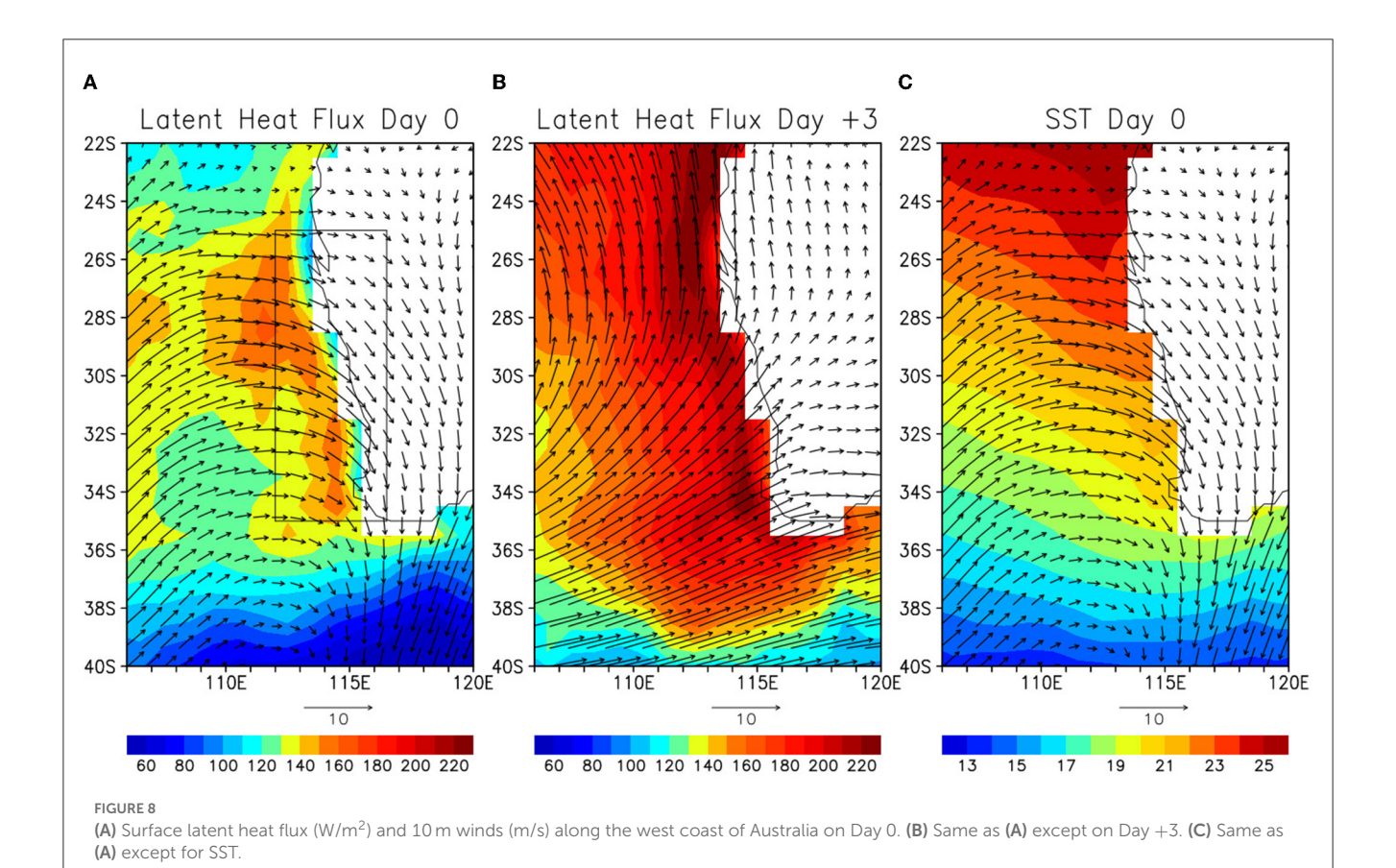
further discussed in the next section.

In summary, significant latent heat fluxes along the west coast of Australia are found during the AR landfalling despite the AR-induced high specific humidity based on the composite analysis. This is because the relatively high SSTs (compared to the west coast of North America) are maintained along the coast by the poleward flowing Leeuwin Current carrying the warm waters from equatorial areas. Because of the rapid changes in specific humidity and persistent strong winds, a substantial change of latent heat fluxes is evident during which ARs pass through the coast.

4. Summary and discussion

This study investigates air-sea fluxes and SSTs associated with atmospheric rivers (ARs) over the southeast Indian Ocean based on the analysis of global data sets of air-sea fluxes and AR characteristics. As demonstrated by a previous study (Shinoda et al., 2019), substantial air-sea fluxes are produced by ARs in the northeast Pacific because of the associated strong winds. In this study, the results for the southeast Indian Ocean are compared with those for the northeast Pacific to identify similarities and differences in AR-induced air-sea fluxes in these regions.

Over the southeast Indian Ocean, SSTs are warmer than areas of the eastern boundary of other ocean basins because of the unique ocean circulations in this region. For example, the Leeuwin Current, one of the major boundary currents in the Indian Ocean, flows poleward against the prevailing equatorward winds and carries warm waters from the tropics. As a result, SSTs along the west coast of Australia are much warmer than coastal areas on the



eastern side of other ocean basins at comparable latitudes. Such different SST fields could cause the different AR-induced air-sea fluxes over the southeast Indian Ocean especially along the coast. Hence, the results in this study are discussed for the open ocean area and coastal region separately.

Over the open ocean area, both case studies and composite analysis for the southeast Indian Ocean indicate large (small) surface evaporation on the western poleward (eastern equatorward) side of ARs where the surface winds are strong (weak) and the near-surface specific humidity is relatively low. The evaporation is small near the center of AR because of the high near-surface specific humidity even though winds are strong.

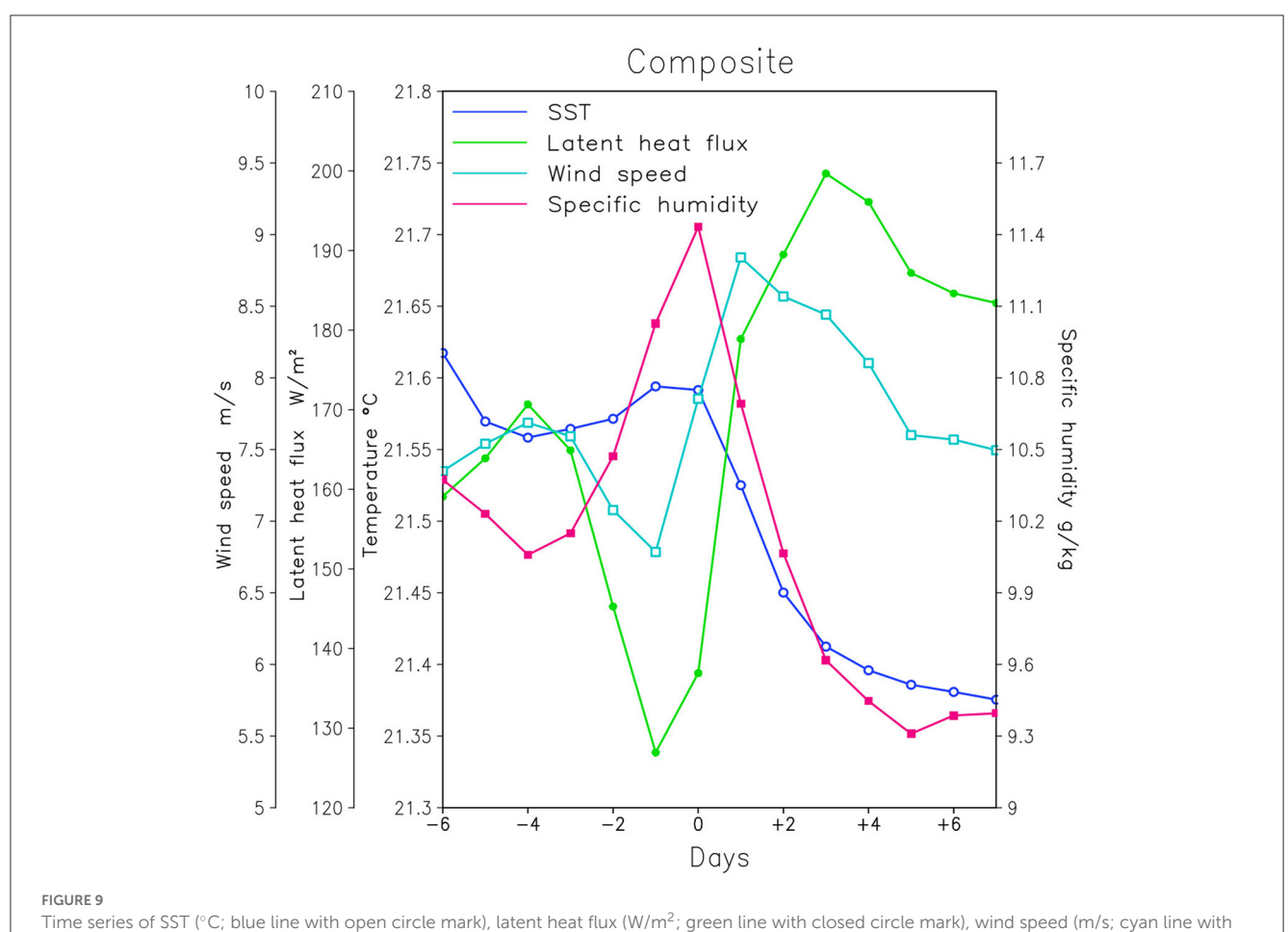
While the large-scale spatial pattern of air-sea fluxes over the southeast Indian Ocean is similar to that in the northeast Pacific, there are some notable differences. For example, the zonal extent of the areas for the large latent heat flux (evaporation) on the western poleward side is larger in the southeast Indian Ocean whereas the large surface evaporation is confined in the narrower regions in the northeast Pacific. This is partly because the zonal component of AR-associated surface winds in the southeast Indian Ocean is stronger than that in the northeast Pacific.

The spatial pattern of SST fluctuations associated with ARs are similar to that of the net surface heat fluxes, suggesting that AR-induced SSTs are primarily generated by surface heat fluxes and vertical processes. The largest component of AR-induced net surface heat flux is the latent heat flux whose spatial pattern is very similar to the net surface heat flux. However, there are some

differences in the spatial pattern between the net surface heat flux and SST variation. For example, the large cooling is found near the center of ARs although the net surface heat flux anomaly is small. This suggests that physical and dynamical processes of the upper ocean may play a significant role in AR-induced SST fluctuations in some areas including heat advection by ocean currents and vertical mixing (entrainment cooling) due to strong winds.

The AR-induced air-sea flux and SST variability along the west coast of Australia are examined based on the composite analysis. Significant latent heat fluxes which exceed 150 W/m² are evident near the coast during the AR landfalling when a large amount of moisture is transported along the coast. Such large latent heat fluxes are not found along the coast of North America at similar latitudes primarily because of cold SSTs caused by the equatorward flowing surface current and upwelling. On the other hand, the poleward flowing Leeuwin Current carries warm waters from the tropics to the west coast of Australia which maintains warm SSTs for all seasons, and thus strong winds around the AR center generate large latent heat fluxes along the west coast of Australia.

Substantial latent heat flux changes during and after the period of AR landfall are evident in the composite. The latent heat flux during the landfall is about 130 W/m^2 (Day -1), and it increases up to about 200 W/m^2 (Day +3) after the landfall, resulting in about 70 W/m^2 changes. Given that annual mean heat fluxes in this region is about 170 W/m^2 (e.g., Feng and Shinoda, 2019), the changes in latent heat flux produced by ARs are significant. Also, since AR-associated strong winds mostly generate the enhancement (more



open square mark), and specific humidity (g/kg; red line with closed square mark) averaged over the area 112°E–116.5°E, 25°S–35°S (a box area in Figure 8A). Ordinates on the left side are for the wind speed (left), latent heat flux (middle) and SST, and the ordinate on the (right) side is for the specific humidity. The positive values of latent heat flux indicate the upward flux (cooling the ocean).

than the reduction) of latent heat flux around this latitude, such latent heat flux variations may influence the mean and longer time scale variability in this region.

In association with the rapid increase of latent heat flux, the SST cooling of about 0.2°C for the 5-day period occurs after the AR landfall. While the results suggest that the SST cooling is caused by the increase of latent heat flux during this period, oceanic processes associated with AR landfalling could contribute to the SST fluctuations (Shinoda et al., 2020). For example, AR-induced winds generate the significant increase in the southward velocity of the Leeuwin Current, and thus the advection of warm waters tends to generate the SST warming. Also, the coastal downwelling caused by the alongshore component of winds could further enhance the SST warming.

The results in this study indicate that the effect of strong surface evaporative cooling exceeds the warming effect caused by ocean dynamics, and thus the rapid SST cooling during Day 0–Day +3 in the composite is caused by the enhanced latent heat flux. However, the cooling rate is largely reduced during Day +3–Day +7 even though the relatively large latent heat flux of 180–190 W/m² is maintained after Day +3. This suggests that oceanic processes may reduce the cooling rate during this period. Since the enhanced Leeuwin Current by ARs is maintained

relatively long time (\sim 10 days) (Shinoda et al., 2020), surface evaporative cooling could be nearly balanced with the warming due to the strong Leeuwin Current. Further analyses including the computation of upper ocean heat budget are necessary for quantifying the relative importance of air-sea fluxes and oceanic processes for controlling SST fluctuations associated with ARs along the coast.

Because of the relatively warm SST maintained by the poleward flowing Leeuwin Current in the southeast Indian Ocean, strong winds caused by synoptic scale atmospheric disturbances such as ARs can generate substantial air-sea fluxes near the coast. While such large surface fluxes on relatively short time scales are often found along the coast in the western boundary where the strong poleward flowing western boundary currents maintain the warm SST, they are rarely found near the coast in midlatitudes of the eastern boundary in other ocean basins because of the cold SSTs. In addition, the strength of the Leeuwin Current varies substantially on the interannual time scale, which largely influences the climate variability in this region such as the Ningaloo Niño (e.g., Feng et al., 2013, 2023; Benthuysen et al., 2014). While a previous study demonstrates substantial changes of surface latent heat flux associated with the Ningaloo Niño due to the interannual variation of SST (Feng and Shinoda, 2019), relatively

short time scale AR-induced air-sea flux events influenced by Ningaloo Niño-associated warm SSTs could also contribute to the interannual variation of air-sea fluxes. For example, the latent heat flux produced by ARs could be enhanced during positive Ningaloo Niño events because of the warmer SSTs, and thus the AR-induced latent heat flux is likely higher than that in normal years. Further studies are necessary to quantify the combined effect of Leeuwin Current variability and AR-induced air-sea fluxes on the interannual variation of air-sea fluxes over the southeast Indian Ocean.

Data availability statement

Publicly available datasets were analyzed in this study. This data can be found here: OAFlux data are available online at: https://oaflux.whoi.edu. CCMP wind data are available online at: https://data.remss.com/ccmp/. SSMI data are available online at: https://www.remss.com/missions/ssmi/.

Author contributions

TS conceived the idea and designed and performed most of the analysis. WH and XF contributed to develop conception of the work through discussions. TS wrote the paper and WH and XF assisted in writing it. All authors contributed to the article and approved the submitted version.

Funding

TS acknowledges support from NASA OVWST Grant 80NSSC23K0982, NOAA Grant NA17OAR4310256, DOD Grants W911NF-20-1-0309 and N00014-22-S-F008, and

NSF Grant OCE 2208273. WH acknowledges NASA OSTST award 80NSSC21K1190.

Acknowledgments

Computing resources were provided by the HPC systems at the Texas A&M University, College Station and Corpus Christi, and the Climate Simulation Laboratory at NCAR's Computational and Information Systems Laboratory, sponsored by the National Science Foundation.

Conflict of interest

The authors declare that the research was conducted in the absence of any commercial or financial relationships that could be construed as a potential conflict of interest.

Publisher's note

All claims expressed in this article are solely those of the authors and do not necessarily represent those of their affiliated organizations, or those of the publisher, the editors and the reviewers. Any product that may be evaluated in this article, or claim that may be made by its manufacturer, is not guaranteed or endorsed by the publisher.

Supplementary material

The Supplementary Material for this article can be found online at: https://www.frontiersin.org/articles/10.3389/fclim.2023. 1150785/full#supplementary-material

References

Atlas, R., Hoffman, R. N., Ardizzone, J., Leidner, S. M., Jusem, J. C., Smith, D. K., et al. (2011). A cross-calibrated, multiplatform ocean surface wind velocity product for meteorological and oceanographic applications. *Bull. Am. Meteorol. Soc.* 92, 157–174. doi: 10.1175/2010BAMS2946.1

Bartusek, S. T., Seo, H., Ummenhofer, C. C., and Steffen, J. D. (2021). The role of nearshore air-sea interactions for landfalling atmospheric rivers on the U.S. West Coast. *Geophys. Res. Lett.* 48, e2020GL091388. doi: 10.1029/2020GL091388

Benthuysen, J., Feng, M., and Zhong, L. (2014). Spatial patterns of warming off Western Australia during the 2011 Ningaloo Niño: Quantifying impacts of remote and local forcing. *Cont. Shelf Res.*, 91, 232–246. doi: 10.1016/j.csr.2014.09.014

Chelton, D. B., Schlax, M. G., Samelson, R. M., and de Szoeke, R. A. (2007). Global observations of large oceanic eddies. *Geophys. Res. Lett.* 34, L15606. doi: 10.1029/2007GL030812

Cresswell, G. R., and Golding, T. J. (1980). Observations of a south-flowing current in the southeastern Indian Ocean. *Deep Sea Res.* 27, 449–466. doi: 10.1016/0198-0149(80)90055-2

Delman, A. S., Lee, T., and Qiu, B. (2018). Interannual to multidecadal forcing of mesoscale eddy kinetic energy in the subtropical southern Indian Ocean. *J. Geophys. Res. Ocean.* 123, 8180–8202. doi: 10.1029/2018JC013945

Dettinger, M. D., Ralph, F. M., Das, T., Neiman, P. J., and Cayan, D. (2011). Atmospheric rivers, floods, and the water resources of California. *Water* 3, 455–478. doi: 10.3390/w3020445

Doyle, J. D., Amerault, C., Reynolds, C. A., and Reinecke, P. A. (2014). Initial condition sensitivity and predictability of a severe extratropical cyclone using a moist adjoint. *Mon. Wea. Rev.* 142, 320–342. doi: 10.1175/MWR-D-13-00201.1

Feng, M., Biastoch, A., Boning, C., Caputi, N., and Meyers, G. (2008). Seasonal and interannual variations of upper ocean heat balance off the west coast of Australia. *J. Geophys. Res.* 113, C12025. doi: 10.1029/2008JC004908

Feng, M., McPhaden, J., Xie, S.-P., and Hafner, J. (2013). La Niña forces unprecedented Leeuwin Current warming in 2011. Sci. Rep. 3, 1–9. doi:10.1038/srep01277

Feng, M., Meyers, G., Pearce, A., and Wijffels, S. (2003). Annual and interannual variations of the Leeuwin Current at 32° S. *J Geophys. Res.* 108, 3355. doi: 10.1029/2002JC001763

Feng, X., and Shinoda, T. (2019). Air-sea flux variability in the southeast Indian Ocean and its relation with Ningaloo Niño. *Front. Marine Sci.* 6, 266. doi: 10.3389/fmars.2019.00266

Feng, X., Shinoda, T., and Han, W. (2023). Topographic trapping of the Leeuwin Current and its impact on the 2010-2011 Ningaloo Niño. *J. Clim.* 36, 1587–1603. doi: 10.1175/JCLI-D-22-0218.1

Gimeno, L., Nieto, R., and Vázquez, M. (2014). Atmospheric rivers: A mini-review. Front. Earth Sci. 2, 1–6. doi: 10.3389/feart.2014.00002

Guan, B., and Waliser, D. E. (2015). Detection of atmospheric rivers: Evaluation and application of an algorithm for global studies. *J. Geophys. Res.-Atmos.* 120, 12514–12535. doi: 10.1002/2015JD024257

Guan, B., Waliser, D. E., and Ralph, F. M. (2018). An inter-comparison between reanalysis and dropsonde observations of the total water vapor transport in individual atmospheric rivers. *J. Hydrometeor.* 19, 321–337. doi: 10.1175/JHM-D-17-0114.1

Guo, Y., Shinoda, T., Guan, B., Waliser, D. E., and Chang, E. K. M. (2020). Statistical relationship between atmospheric rivers, extratropical cyclones, and anticyclones. *J. Clim.* 33, 7817–7834. doi: 10.1175/JCLI-D-19-0126.1

Hirota, N., Takayabu, Y. N., Kato, M., and Akane, S. (2016). Roles of an atmospheric river and a cutoff low in the extreme precipitation event in hiroshima on 19 August 2014. *Mon. Wea. Rev.* 144, 1145–1160. doi: 10.1175/MWR-D-15-0299.1

Kataoka, T., Tozuka, T., and Yamagata, T. (2017). Generation and decay mechanisms of ningaloo niño/niña. *J. Geophys. Res. Ocean.* 122, 8913–8932. doi: 10.1002/2017JC012966

Kim, H.-., M., and Alexander, M. A. (2015). ENSO's modulation of water vapor transport over the Pacific–North American region. *J. Clim.* 28, 3846–3856. doi: 10.1175/JCLI-D-14-00725.1

Mears, C., Lee, T., Ricciardulli, L., Wang, X., and Wentz, F. (2022a). Improving the accuracy of the cross-calibrated multi-platform (CCMP) ocean vector winds. *Remote Sens.* 14, 4230. doi: 10.3390/rs14174230

Mears, C., Lee, T., Ricciardulli, L., Wang, X., and Wentz, F. (2022b). RSS Cross-Calibrated Multi-Platform (CCMP) 6-hourly ocean vector wind analysis on 0.25 deg grid. Version 3.0, Remote Sensing Systems, Santa Rosa, CA. doi: 10.56236/RSS-uv6h30

Mundhenk, B. D., Barnes, E., and Maloney, E. (2016). All-season climatology and variability of atmospheric river frequencies over the north Pacific. *J. Clim.* 29, 4885–4903. doi: 10.1175/JCLI-D-15-0655.1

Neiman, P. J., Ralph, F. M., Wick, G. A., Lundquist, J., and Dettinger, M. D. (2008). Meteorological characteristics and overland precipitation impacts of atmospheric rivers affecting the West Coast of North America based on eight years of SSM/I satellite observations. *J. Hydrometeor.* 9, 22–47. doi: 10.1175/2007JHM 855.1

Persson, P. O. G., Neiman, P. J., Walter, B., Bao, J. W., and Ralph, F. M. (2005). Contributions from California coastal-zone surface fluxes to heavy coastal

precipitation: A CALJET case study During the Strong El Niño of 1998. Mon. Wea. Rev. 133, 1175–1198. doi: 10.1175/MWR2910.1

Ralph, F. M., Neiman, P. J., and Rotunno, R. (2005). Dropsonde observations in low-level jets over the northeastern pacific ocean from CALJET-1998 and PACJET-2001: mean vertical-profile and atmospheric-river characteristics. *Mon. Wea. Rev.* 133, 889–910. doi: 10.1175/MWR2896.1

Ralph, F. M., Neiman, P. J., Wick, G. A., Gutman, S. I., Dettinger, M. D., Cayan, D. R., et al. (2006). Flooding on California's Russian River: Role of atmospheric rivers. *Geophys. Res. Lett.* 33, L13801. doi: 10.1029/2006GL026689

Reynolds, C. A., Doyle, J. D., Ralph, M. F., and Demirdian, R. (2019). Adjoint sensitivity of north pacific atmospheric river forecasts. *Mon. Wea. Rev.* 147, 1871–1897. doi: 10.1175/MWR-D-18-0347.1

Shinoda, T., Han, W., Zamudio, L., and Feng, X. (2020). Influence of atmospheric rivers on the Leeuwin Current system. *Clim. Dyn.* 54, 4263–4277. doi: 10.1007/s00382-020-05228-z

Shinoda, T., Zamudio, L., Guo, Y., Metzger, E. J., and Fairall, C. (2019). Ocean variability and air-sea fluxes produced by atmospheric rivers. *Sci. Rep.* 9, 1–12. doi: 10.1038/s41598-019-38562-2

Smith, B. L., Yuter, S. E., Neiman, P. J., and Kingsmill, D. E. (2010). Water vapor fluxes and orographic precipitation over northern California associated with a land-falling atmospheric river. *Mon. Wea. Rev.* 138, 74–100. doi: 10.1175/2009MWR2939.1

 $Waliser, D.\ E., and\ Guan, B.\ (2017).\ Extreme\ winds\ and\ precipitation\ during\ landfall\ of\ atmospheric\ rivers.\ Nature\ Geosci.\ 10,179-183.\ doi: 10.1038/ngeo2894$

Yu, L., Jin, X., and Weller, R. A. (2008). Multidecade Global Flux Datasets from the Objectively Analyzed Air-sea Fluxes (OAFlux) Project: Latent and Sensible Heat Fluxes, Ocean Evaporation, and Related Surface Meteorological Variables. Massachusetts: Woods Hole Oceanographic Institution. OAFlux Project Technical Report. OA-2008–OA-2001.

Zhu, Y., and Newell, R. E. (1998). A proposed algorithm for moisture fluxes from atmospheric rivers. *Mon. Wea. Rev.* 126, 725–735. doi: 10.1175/1520-0493(1998)126<0725:APAFMF>2.0.CO;2